Figure 1. Meteosat retrieval of dust visible optical depth over the North Atlantic and Mediterranean. Yellows and reds indicate high optical depths. From *Dulac et al.*[1996].
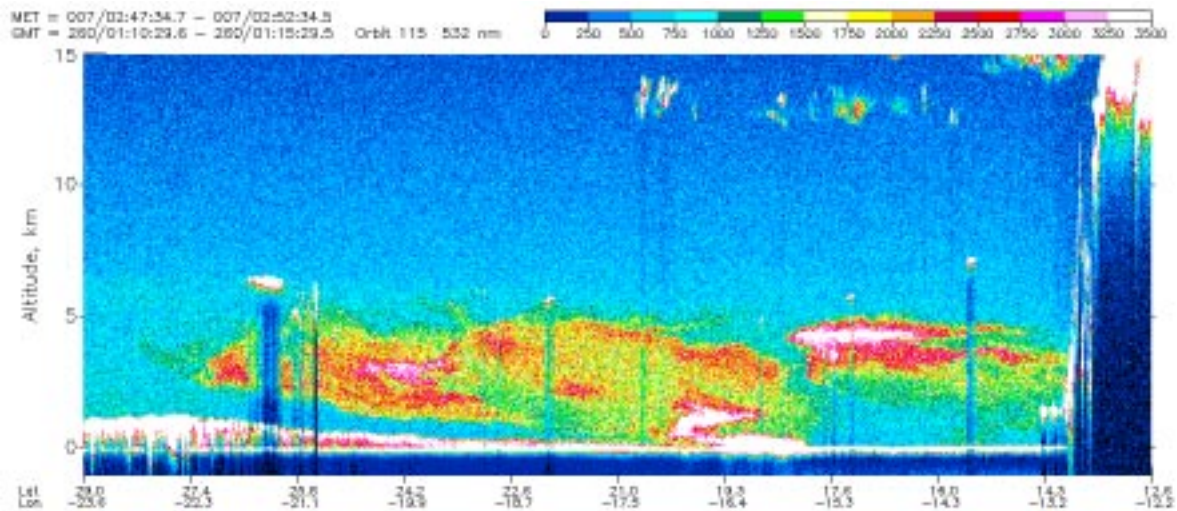

Figure 2. LITE backscatter retrieval illustrating the vertical structure of the Saharan dust plume. The edge of the continent is on the right side of the figure, at approximately -16.4 longitude. Note the elevated dust layer (the yellows and reds) as the plume advects over the ocean. Also visible are higher altitude clouds and other aerosols near the surface toward the northwest (left) side of the figure. From http://www-arb.larc.nasa.gov/lite.
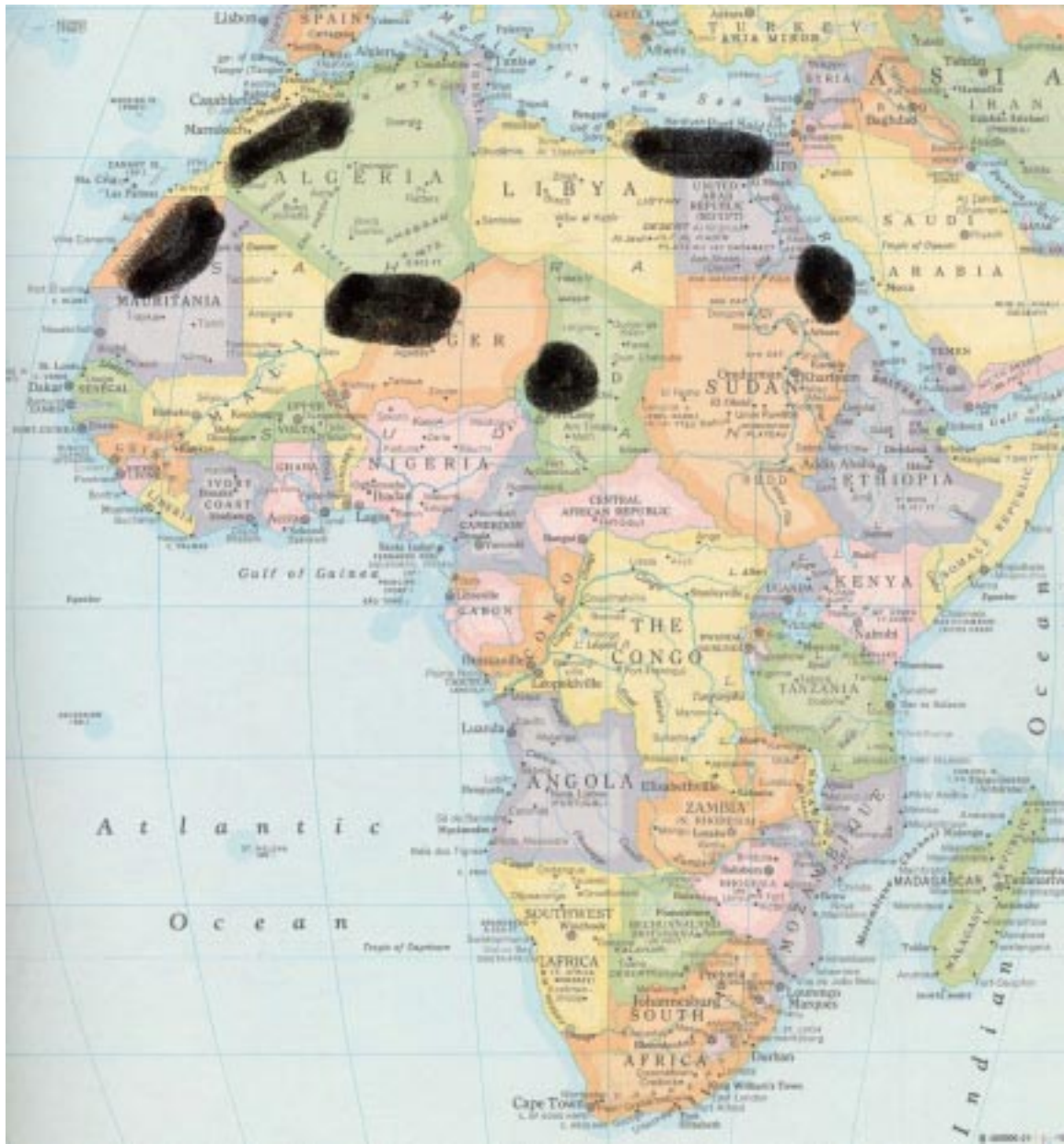
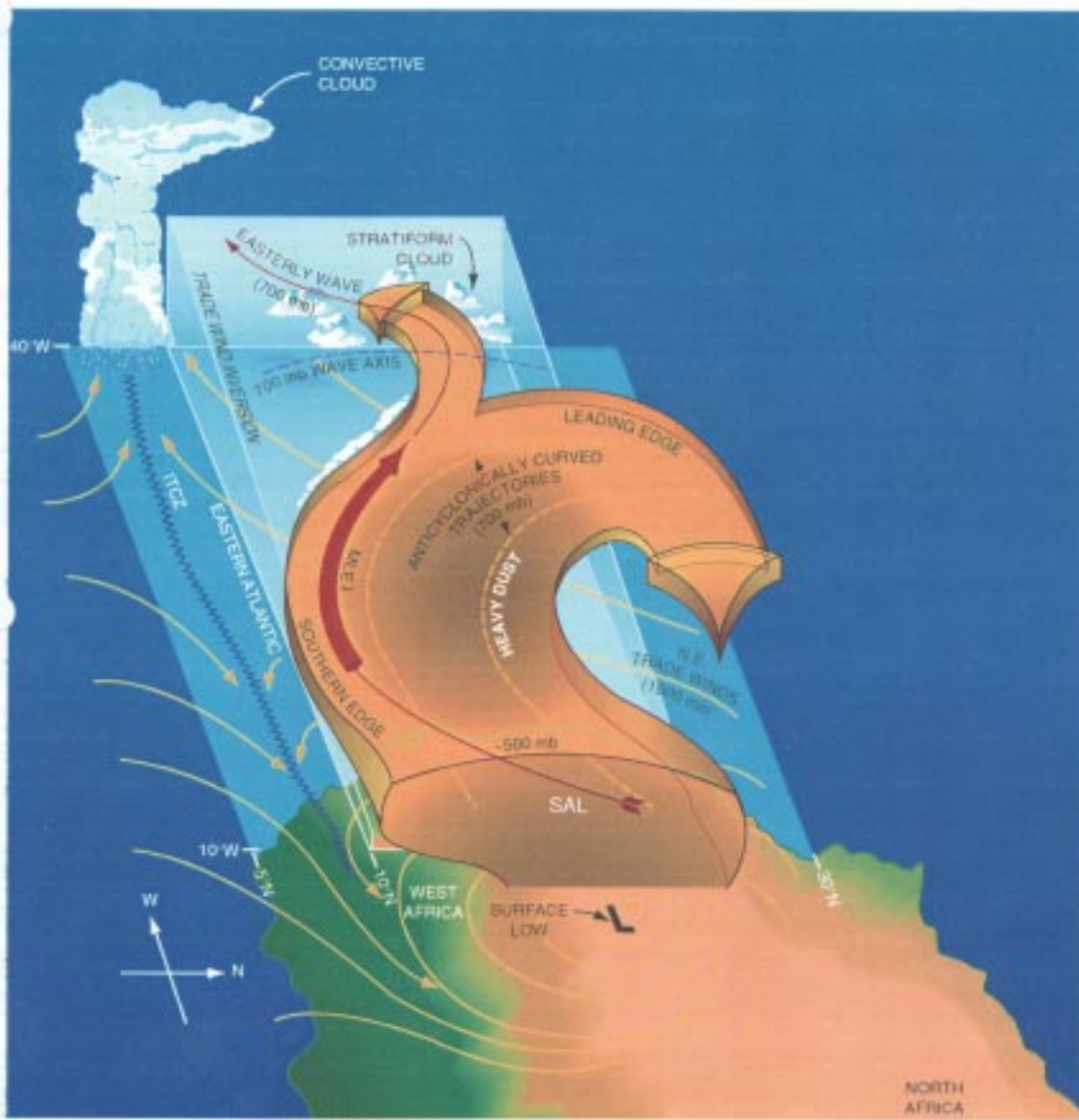Figure 3. Location of major dust source regions in North Africa.

Figure 4. Conceptual model of the Saharan Air Layer and the dust plume advecting west off the continent. From *Karyampudi et al.* [1999].
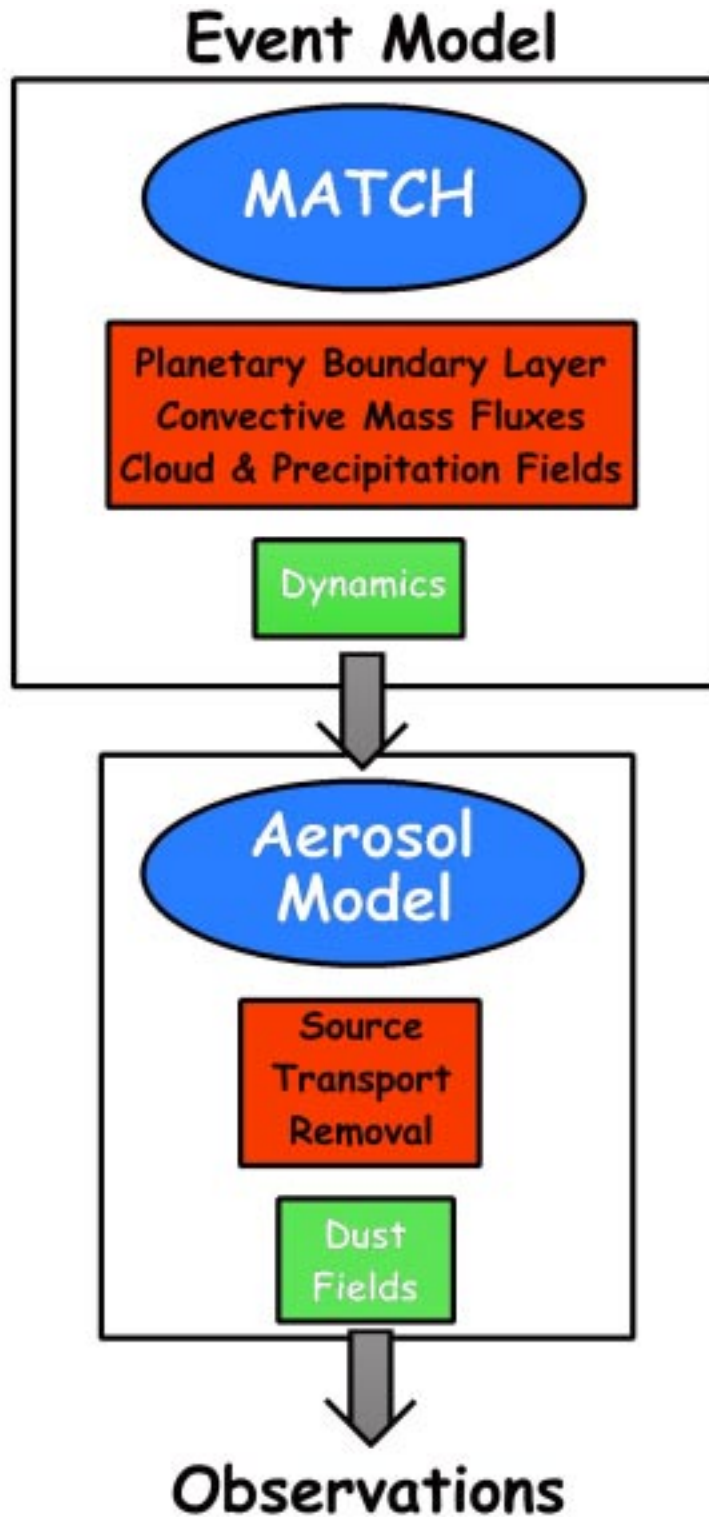
Event Model

MATCH

Planetary Boundary Layer
Convective Mass Fluxes
Cloud & Precipitation Fields

Dynamics

Aerosol Model

Source
Transport
Removal

Dust Fields

Observations

Figure 5. Schematic of the coupled dynamical/aerosol model. Observed meteorology fed into the dynamical component drive the aerosol model. Predicted dust fields may then be compared with observations.
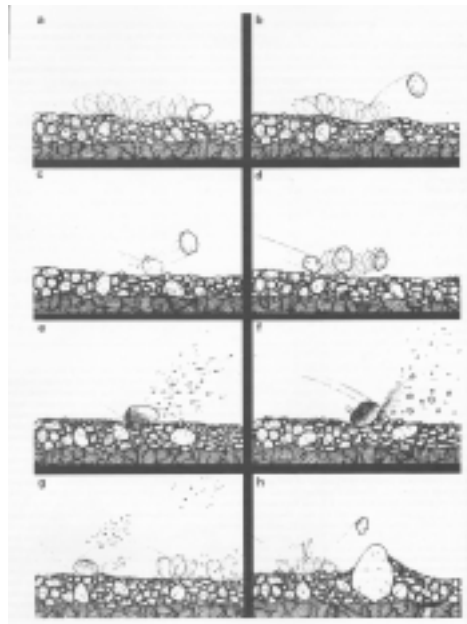
Figure 6. Illustration of the sandblasting process, where large surface aggregates are mobilized to bounce across the surface ("slatation"), causing the emission of finer grained particles [from *Gillette*, 1981].
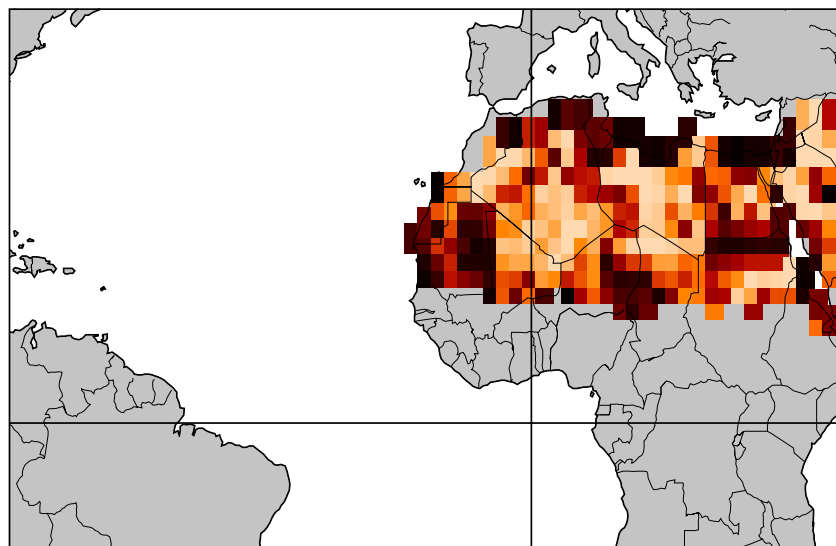

Figure 7. Modeled domain, indicating satellite derived source regions used to calculate where dust is lifted from. The fraction represents the total fraction of the grid cell available as a source area.

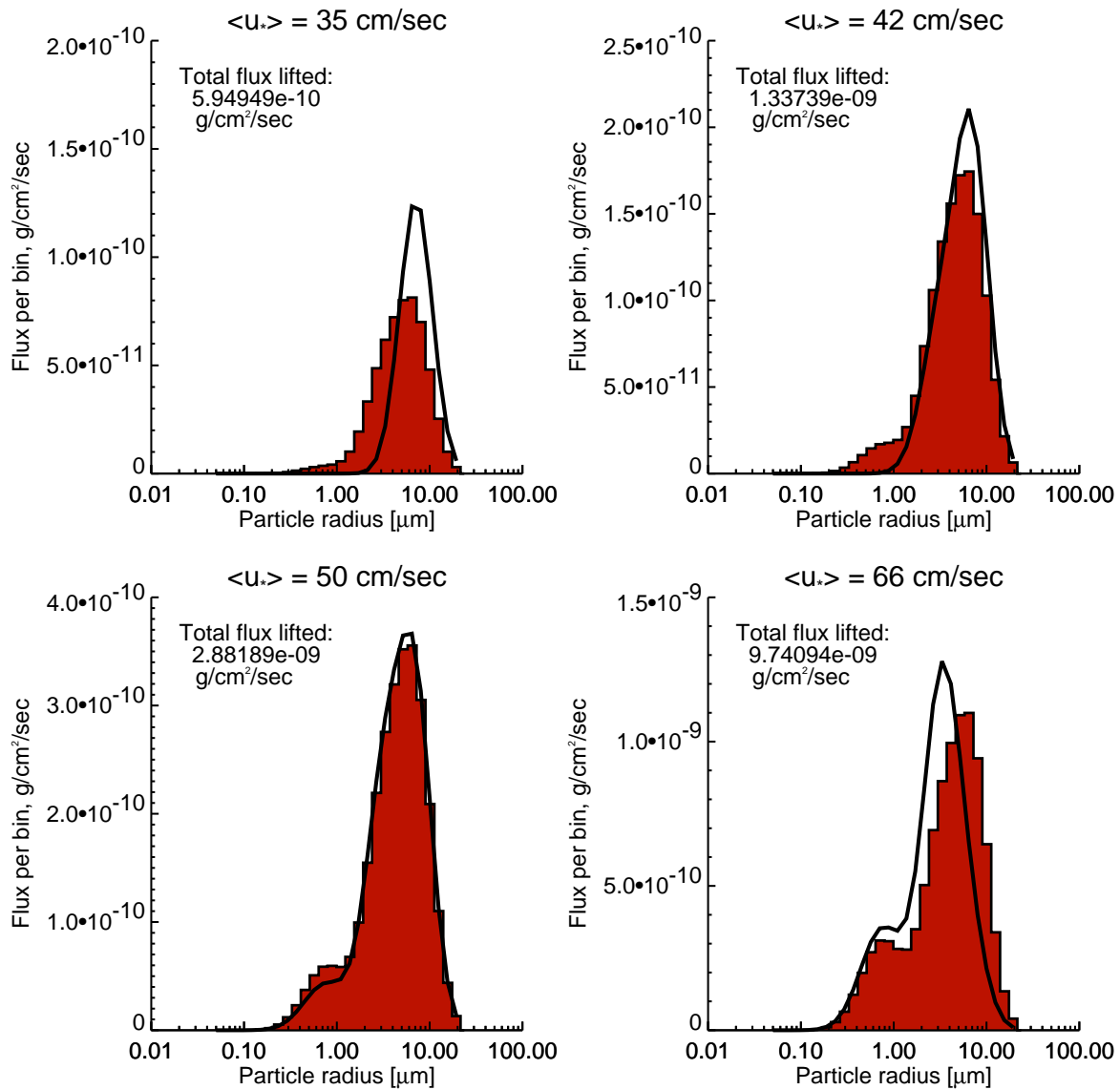# Variation of Emitted Size Distribution with Friction Speed

Figure 8. This figure illustrates the mass lifting rate and size partitioning of the dust predicted in the model as it varies with the mean friction velocity. The histogram represents the modeled size partitioning. The solid curve represents the observations of *Alfaro et al.* [1998]. Discrepancies may be attributed to our simplified treatment of the detailed sandblasting process.
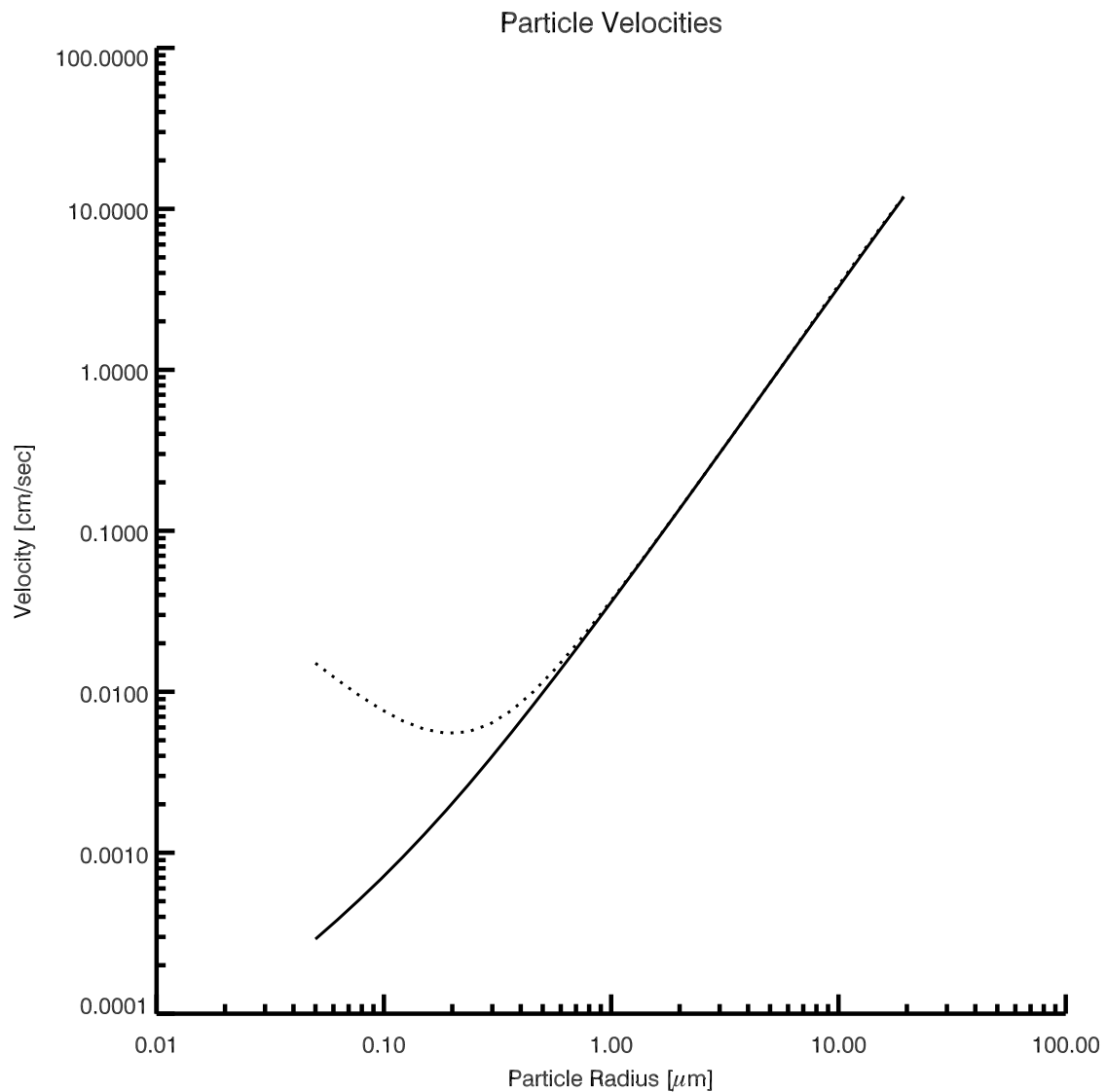
Figure 9. This figure shows the modeled fall velocity as a function of particle radius. The solid curve is the sedimentation velocity; the dashed curve is the deposition velocity used in the lowest model layer. At large particle sizes the curves are coincident, indicating the dominance of the gravitational settling term. At the smallest particle sizes the deposition velocity far exceeds the gravitational settling term, indicating the importance of Brownian diffusion at these sizes.
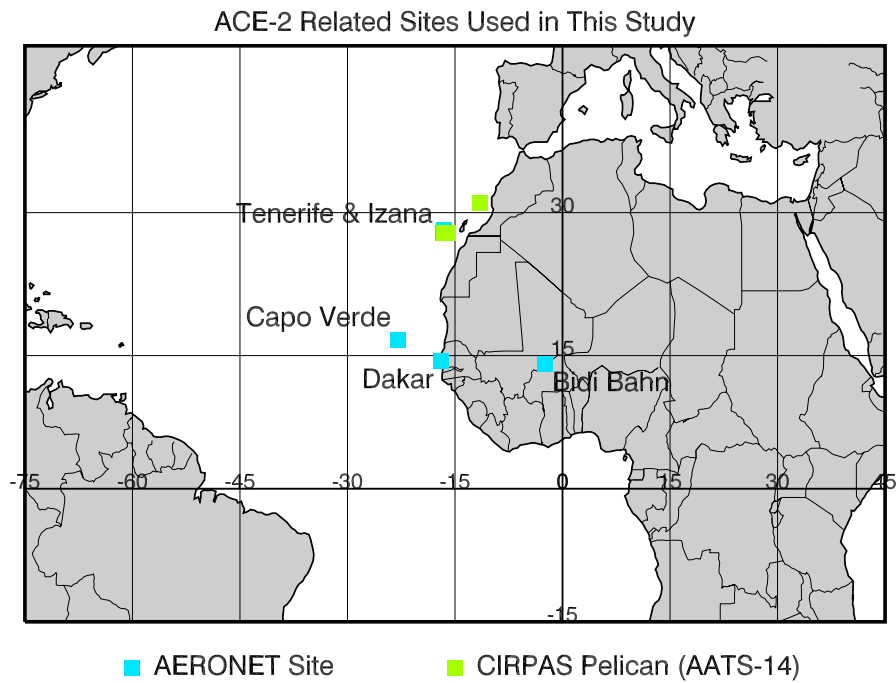
Figure 10. Location of AERONET sites and Pelican flights used for validation in our model.
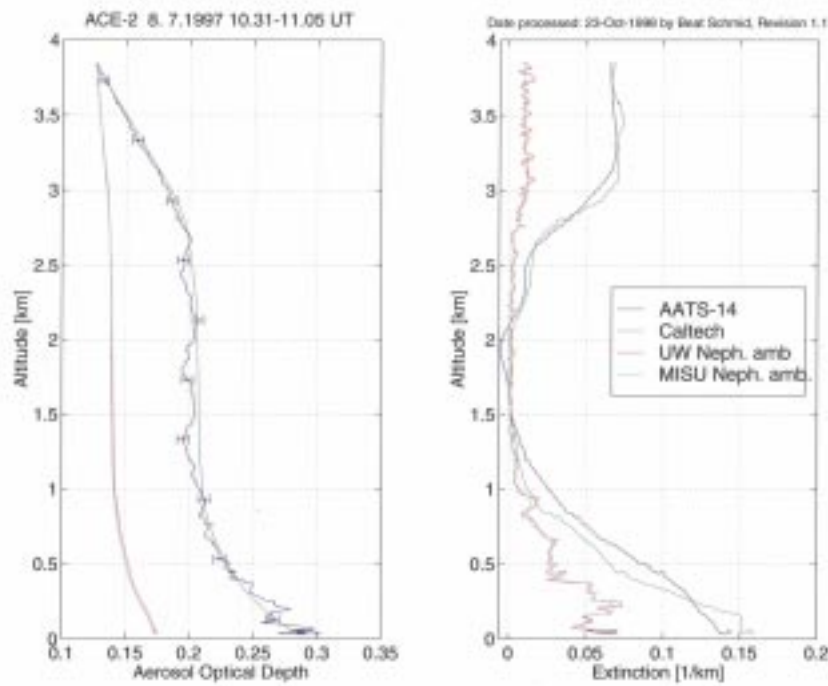
Figure 11. Optical depth and extinction profiles obtained from the NASA AATS-14 during a vertical profile flown on the Pelican aircraft. The figure shows comparisons to the profiles obtained with particle counters.
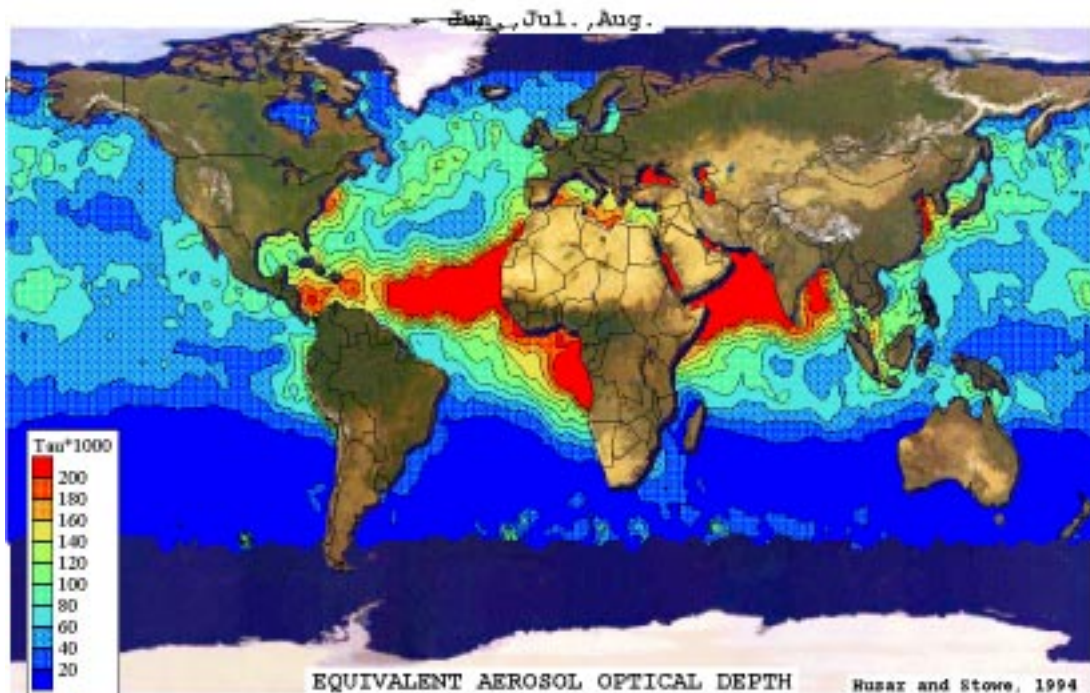
Figure 12. AVHRR seasonal average (JJA 1988) aerosol optical depth retrieval. Clearly visible are the signals from Saharan dust, biomass burning (southwest Africa), and dust and pollutants from the Arabian Peninsula and India.
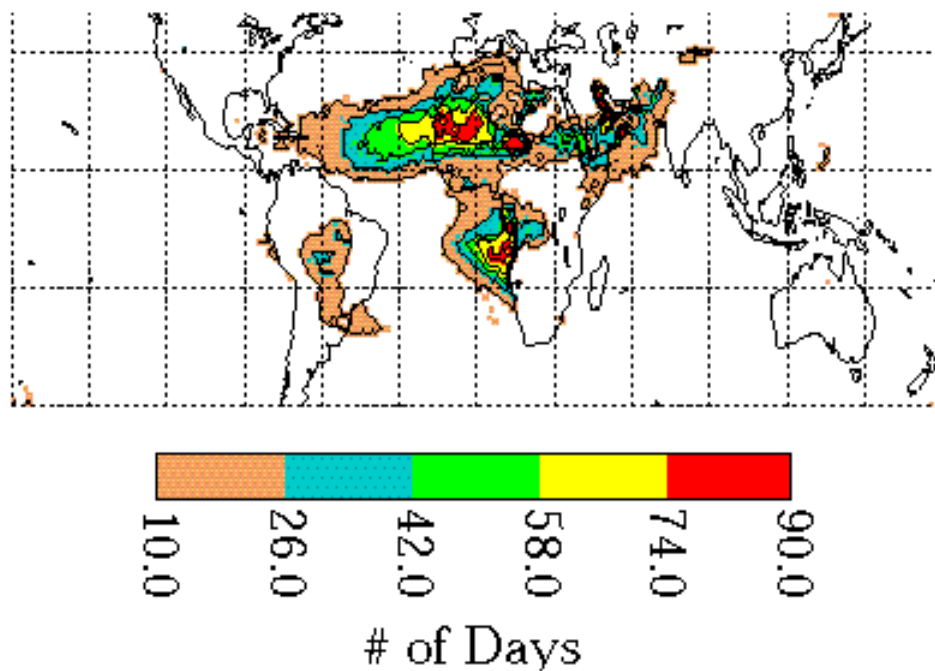
Figure 13. TOMS Aerosol Index retrievals, indicating the frequency of coverage by UV absorbing aerosols (dust and smoke) for the period of July, August, and September 1988.

Figure 14a.

Total mass lifted, June 18 - July 18, 1997

Mass lifted [g/m²]

| 1 | 2 | 5 | 10 | 20 | 50 | 100 |

Total Mass Lifted: 235 tg
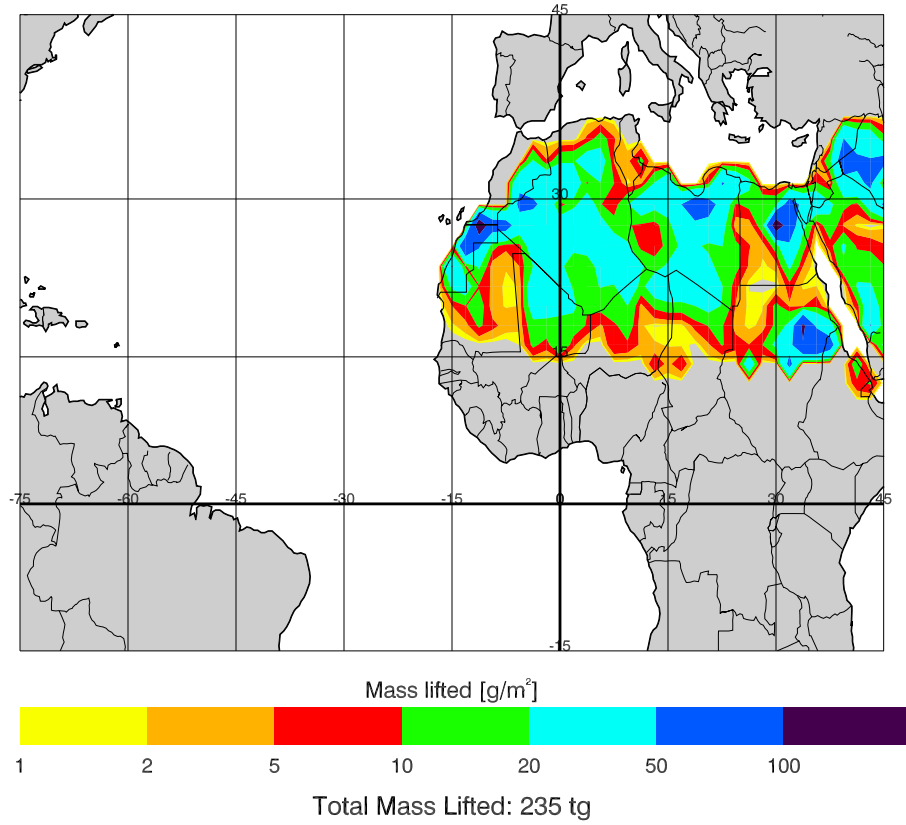
Figure 14b.

Cycle of Dust Mobilization, ACE II Simulation

Domain Integrated Mass Lifting Rate (kg/sec)

July 1997 (0000 UTC)
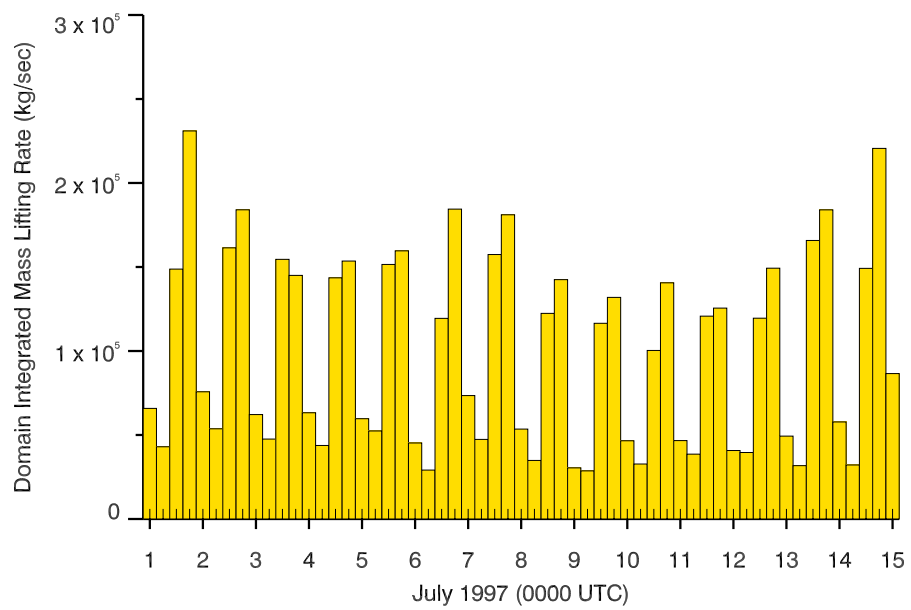
Predicted Dust Fluxes, 1800 UTC

Figure 14c.

Dust Flux [g cm^{-2} s^{-1}]

10^{-10} 10^{-9} 10^{-8}
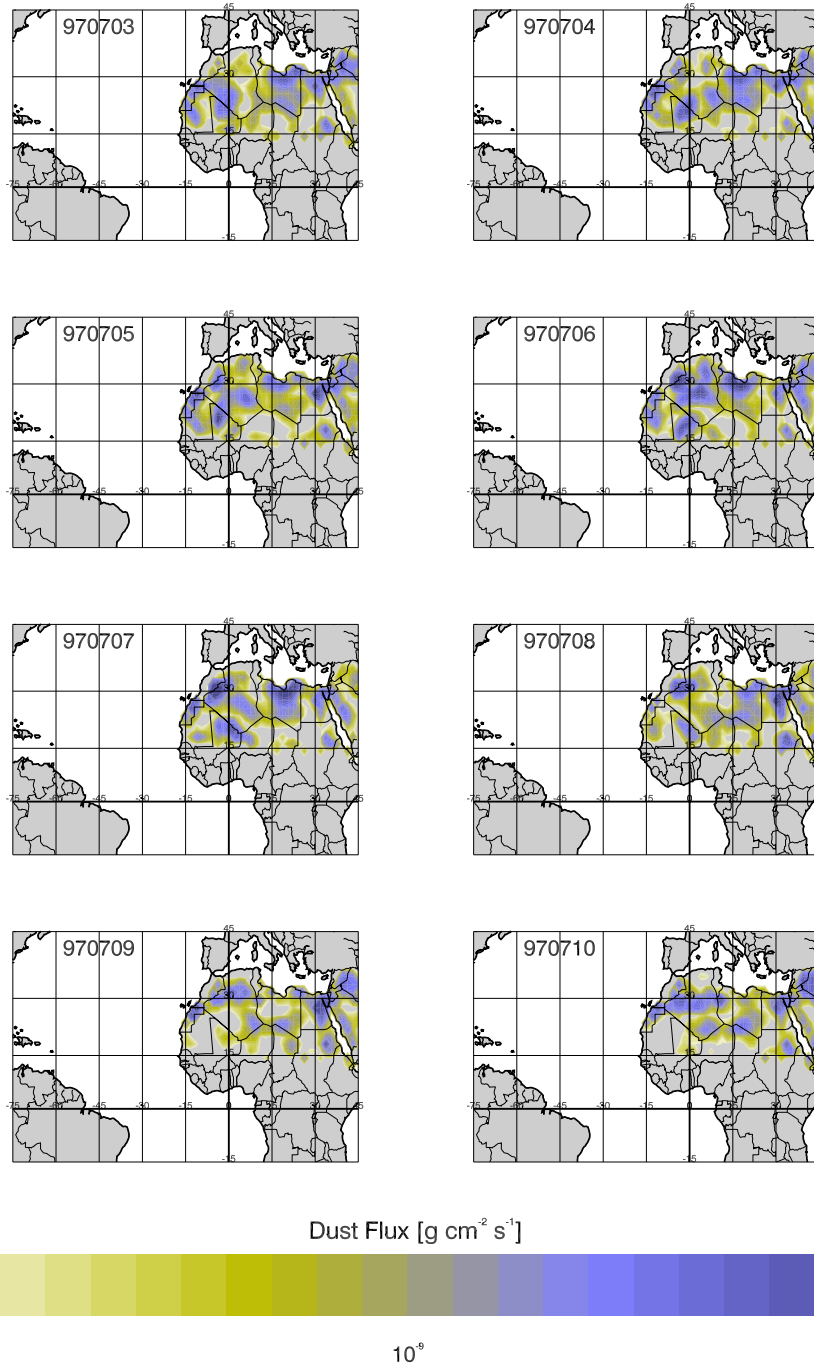
Figure 14. Dust fluxes predicted for the model base case simulation. Total mass lifted is 235 tg (a). The pattern of emissions shows a diurnal signal, indicating maximum dust lifting in the afternoons (b). Figure (c) shows the variation of source regions as a function of time.
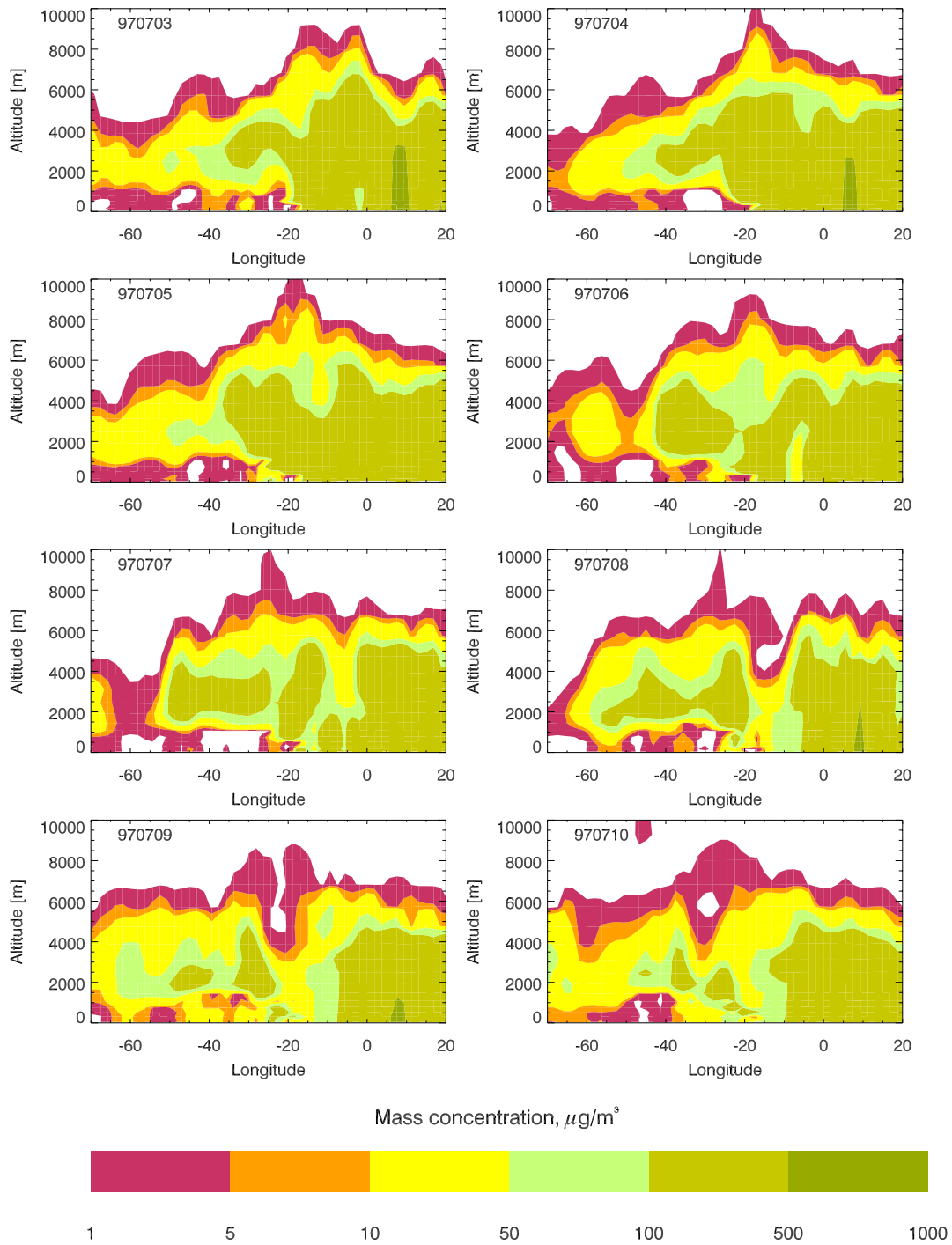
Figure 15. Meridional cross section of simulated dust mass concentrations for the base model run.

Dust Aerosol Column Mass Loading, July 3-10, 1997, 1800 UTC
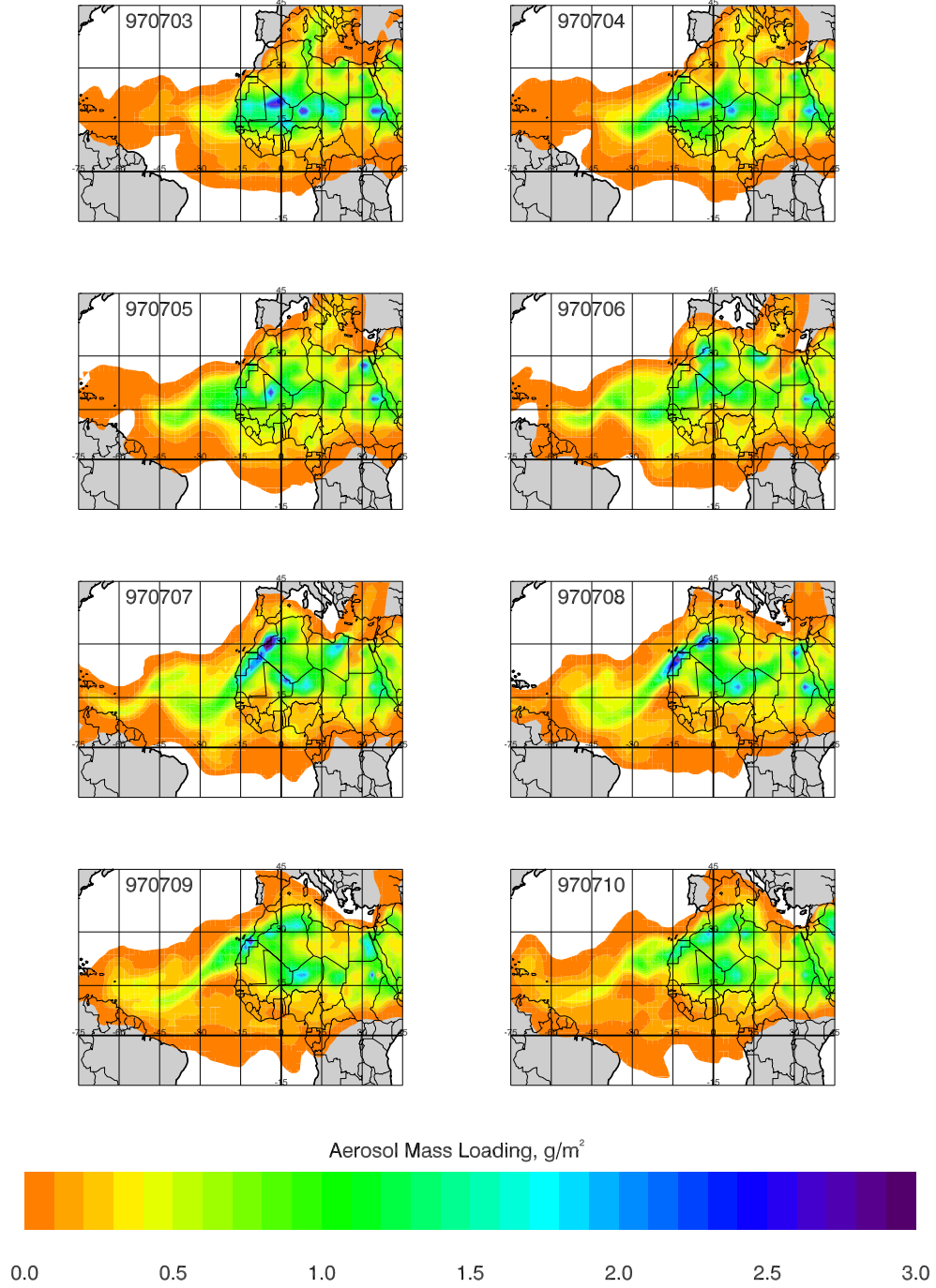
Figure 16. Modeled aerosol column densities for the base simulation run.

TOMS UV Absorbing Aerosol Index, July 3-10, 1997
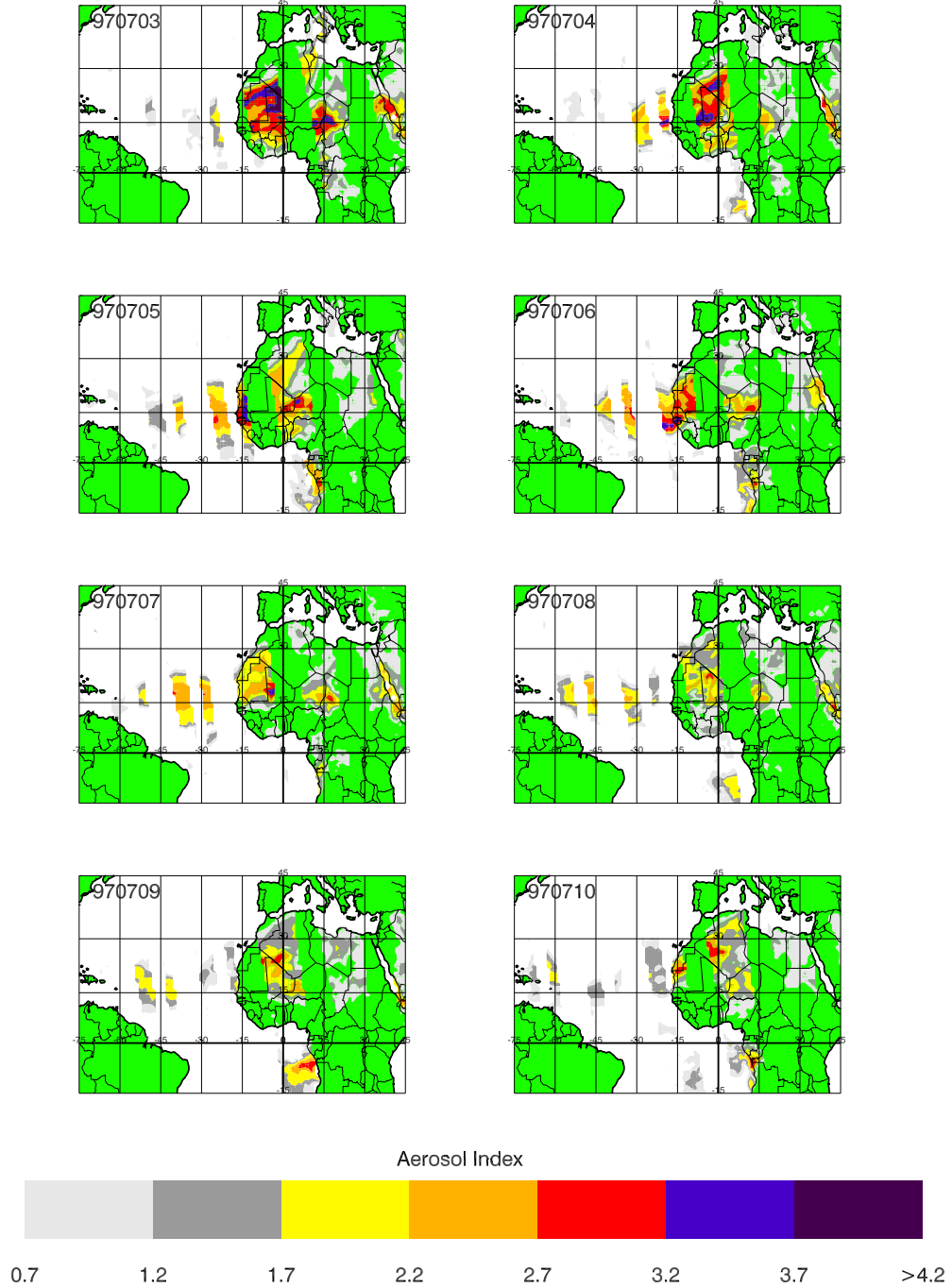
Figure 17. TOMS Aerosol Index retrievals for July 3-10, 1997.
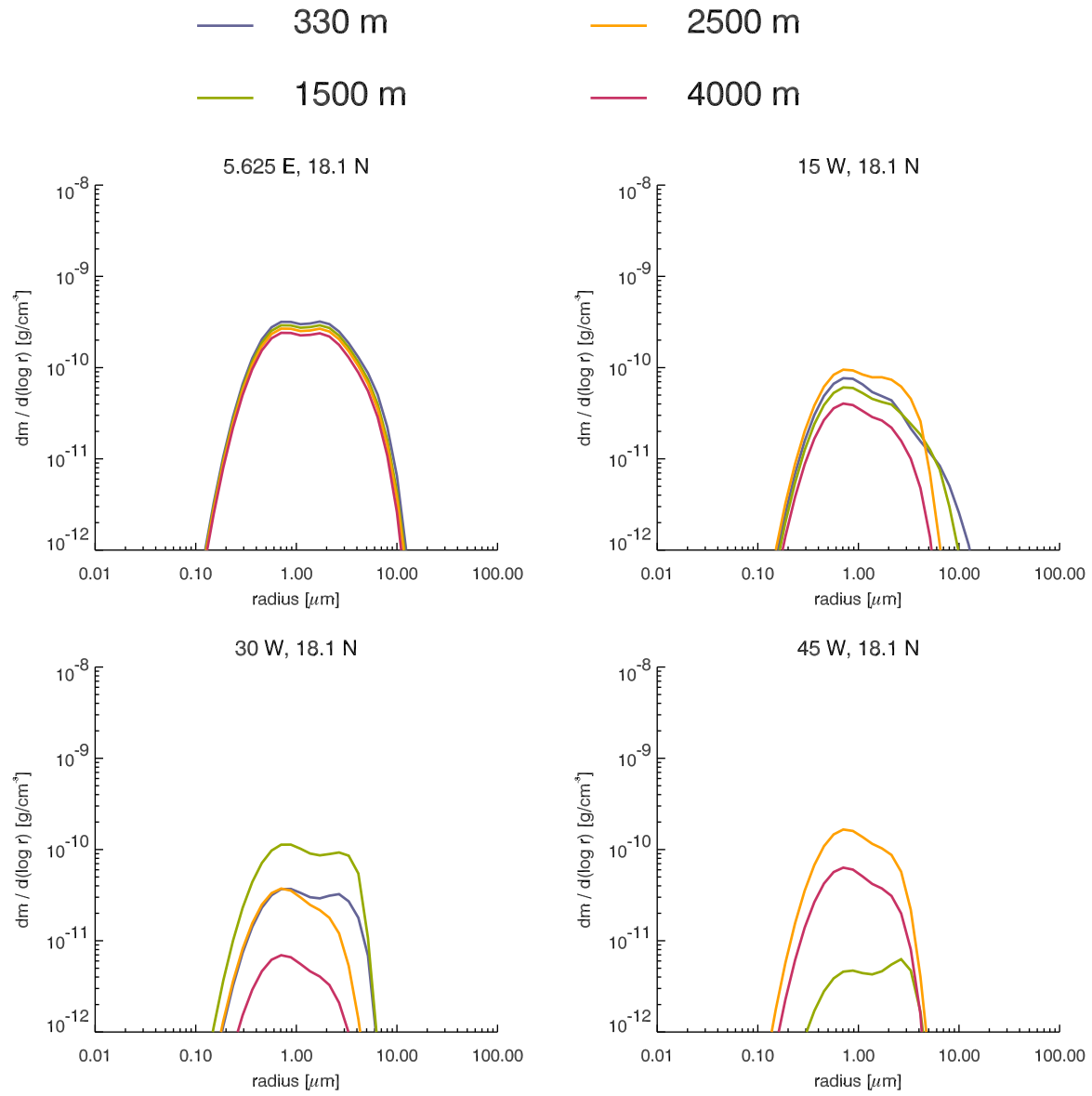
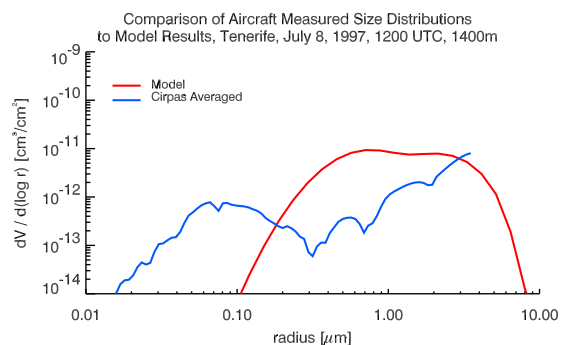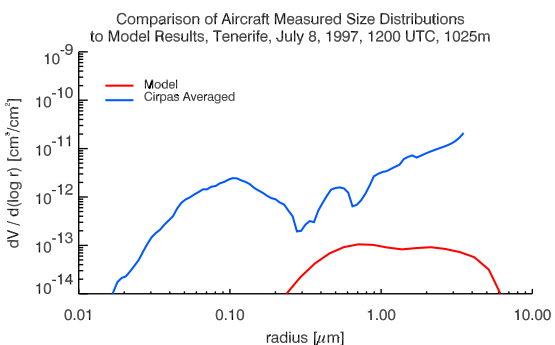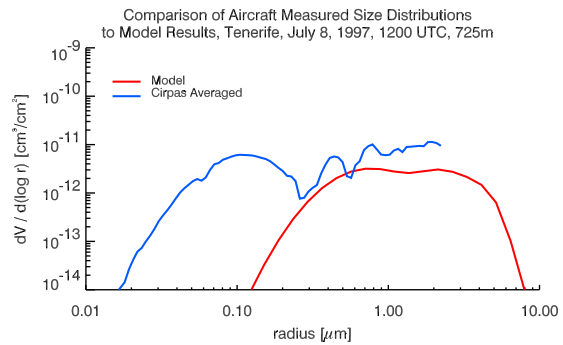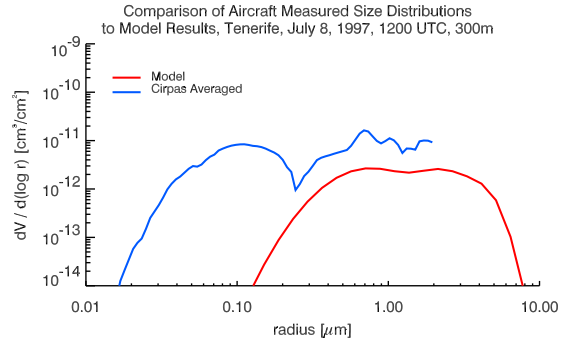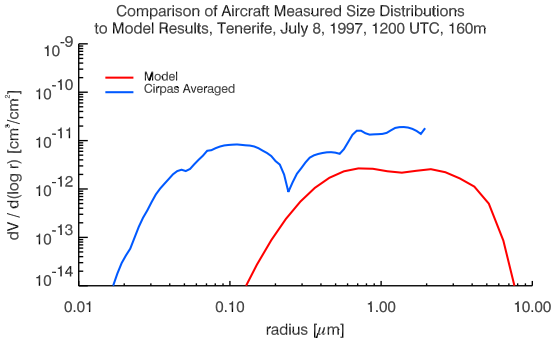Figure 18. Modeled size distributions for July 10 at 18.1 N.
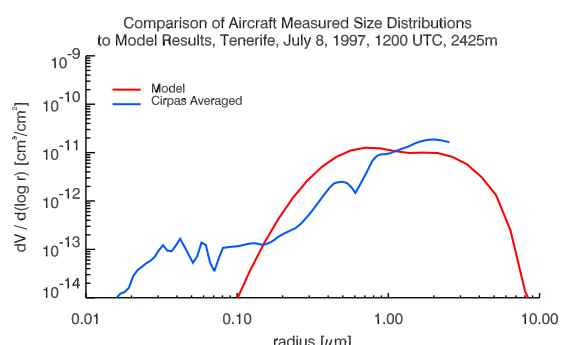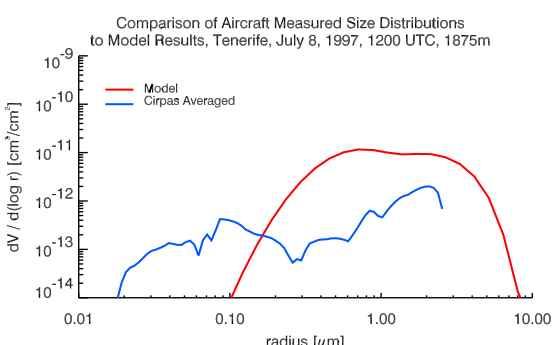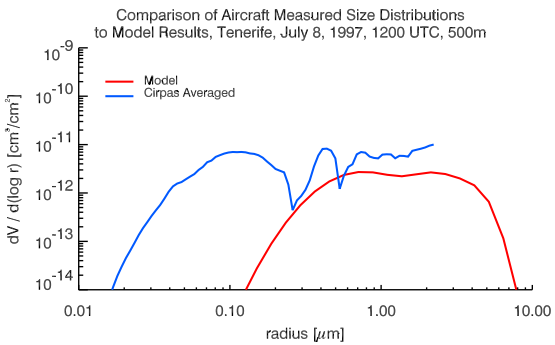
Figure 19. Comparison of modeled to CIRPAS measured size distributions on a vertical profile flown July 8.
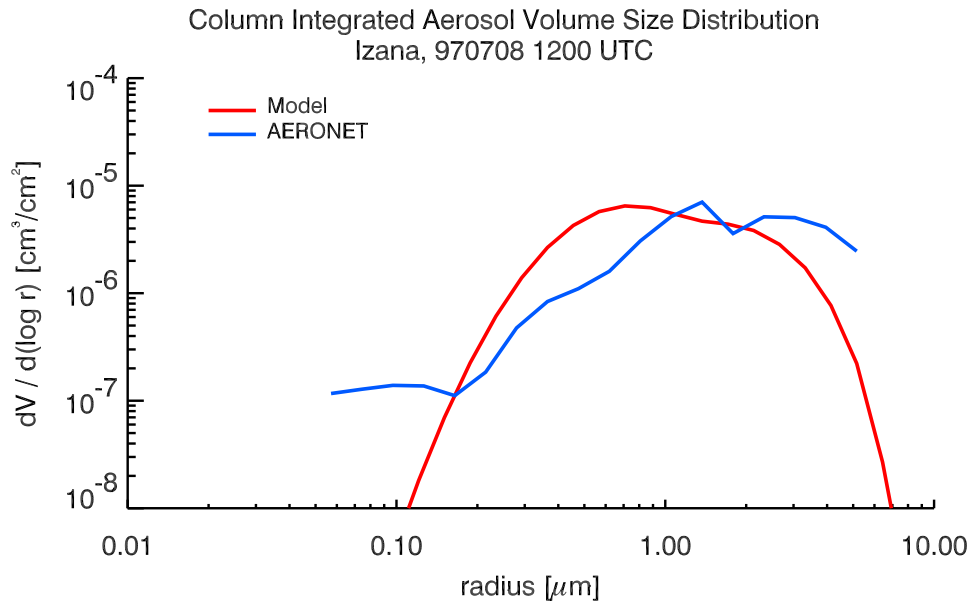
Column Integrated Aerosol Volume Size Distribution
Izana, 970708 1200 UTC

Figure 20. Comparison of modeled to AERONET retrieved size distribution (column integrated) over Izana.

Comparison of AATS-14 Optical Depth Profile
to Model Results, Tenerife, July 8, 1997

Comparison of AATS-14 Extinction Profile
to Model Results, Tenerife, July 8, 1997

(a)   (b)
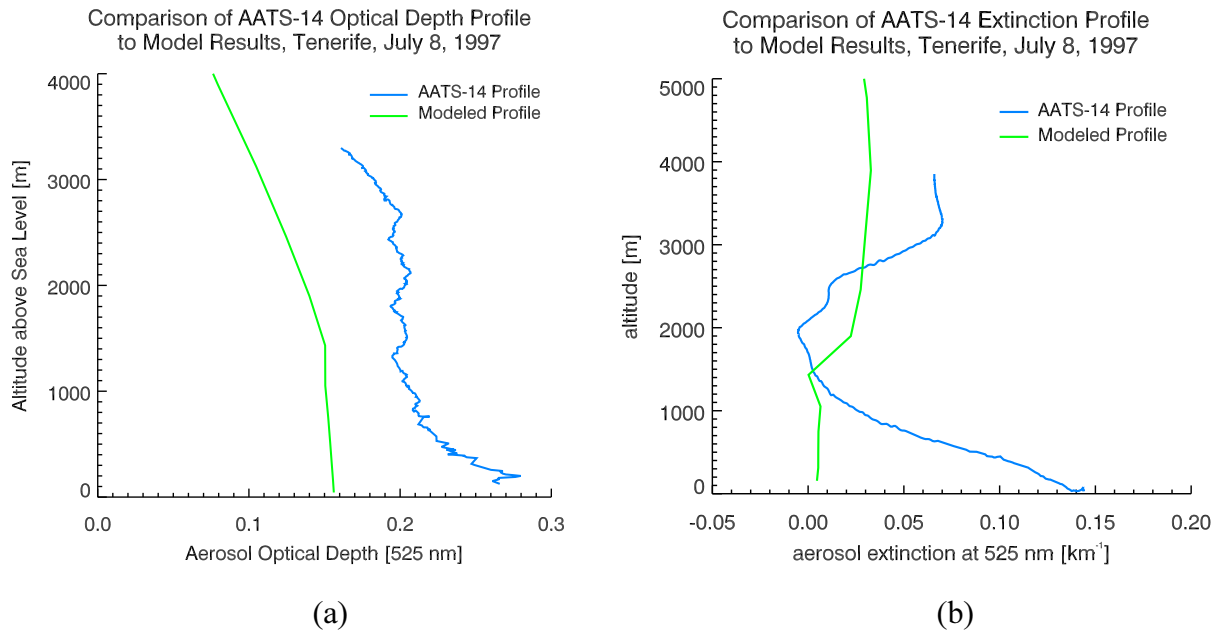
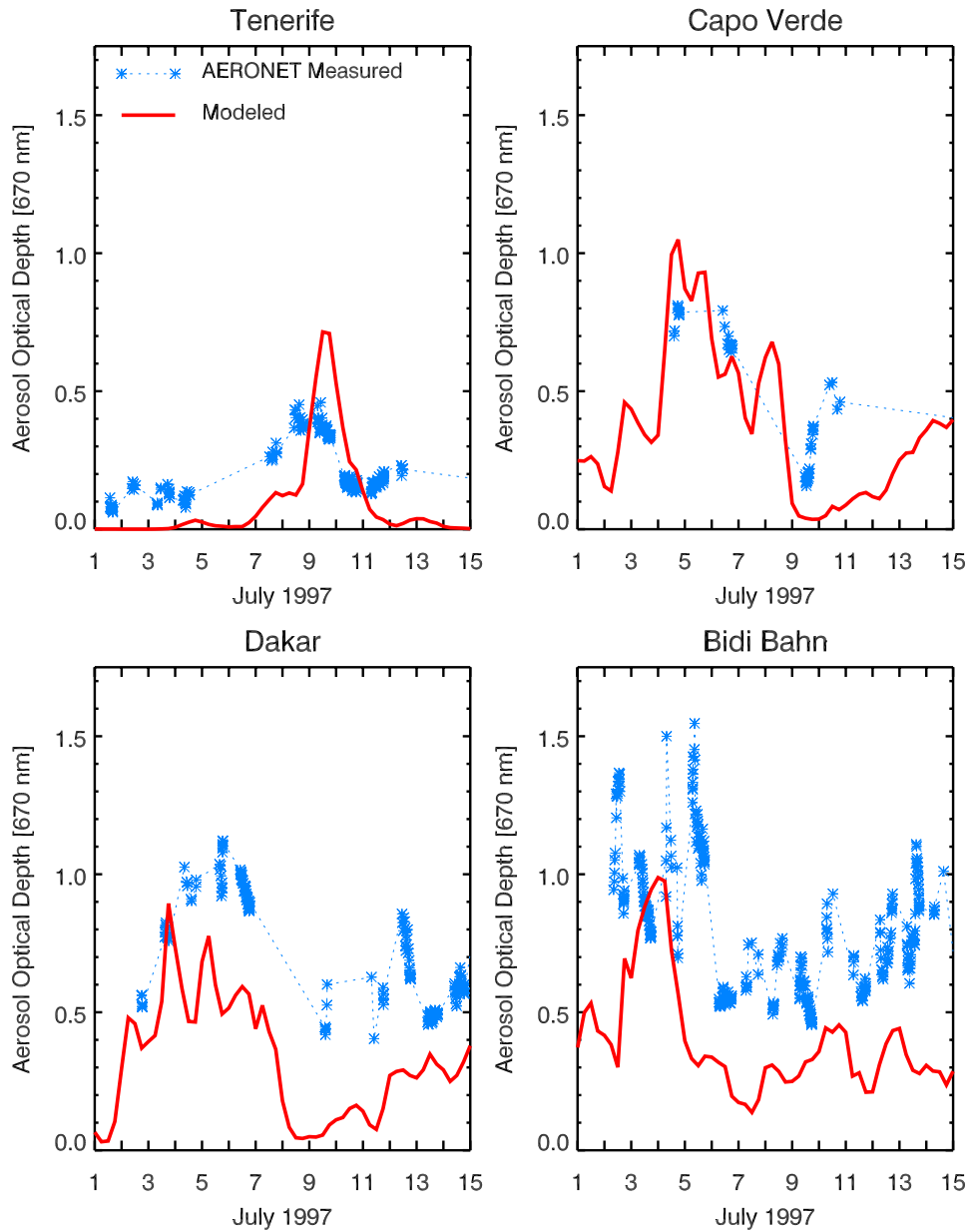Figure 21. Comparison of modeled to CIRPAS retrieved optical depth and extinction profiles near Tenerife, July 8.

Figure 22. Comparison of modeled to AERONET retrieved optical depths for July 1-15.

Computed Daily Average Dust Optical Depth

Figure 23a.

630 nm AOD, July 3-10, 1997
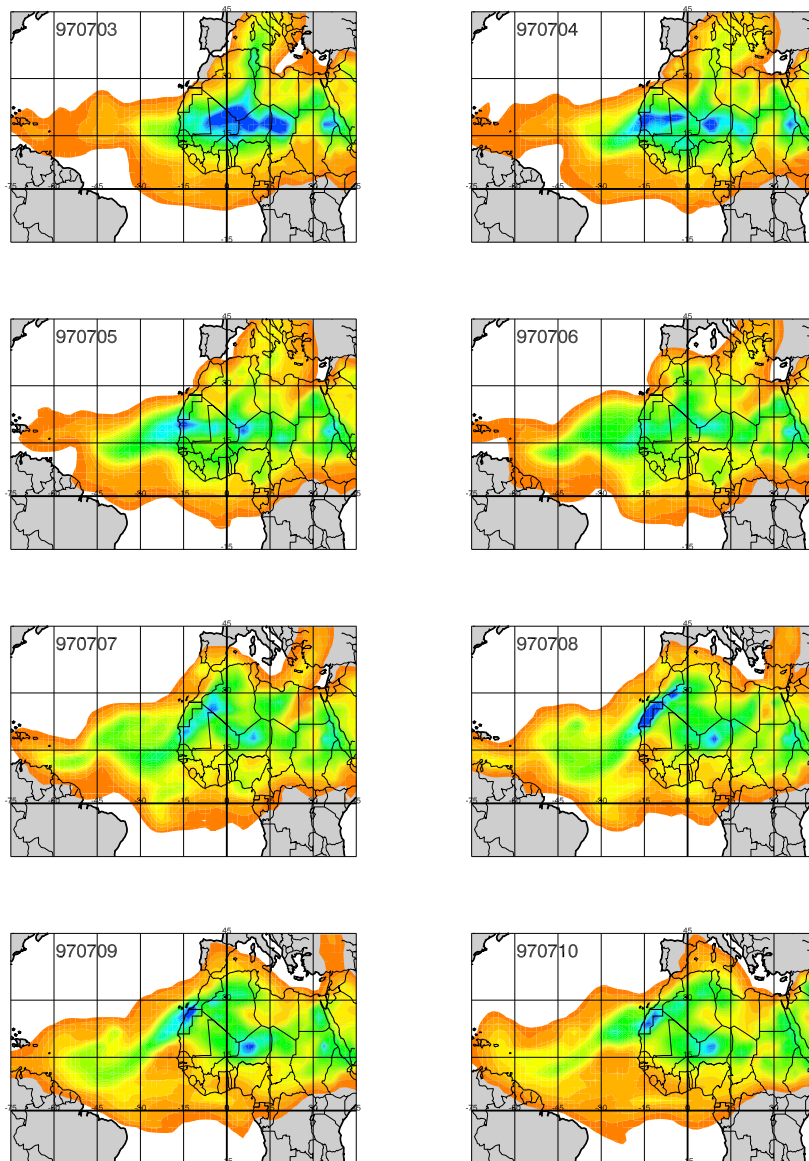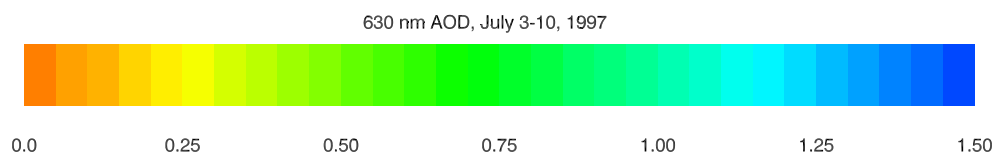
Figure 23a. Modeled 630 nm optical depths, July 3-10.
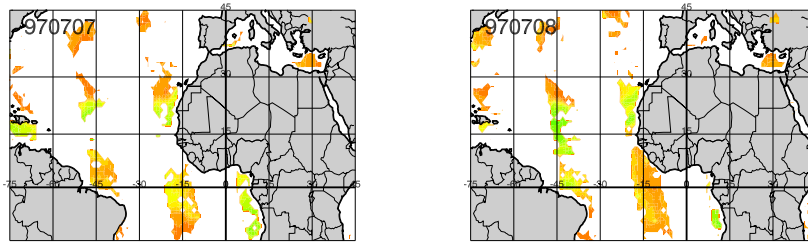
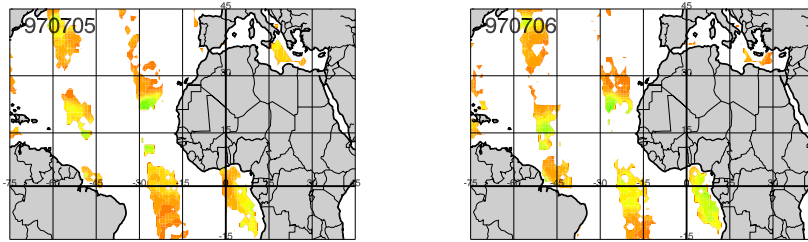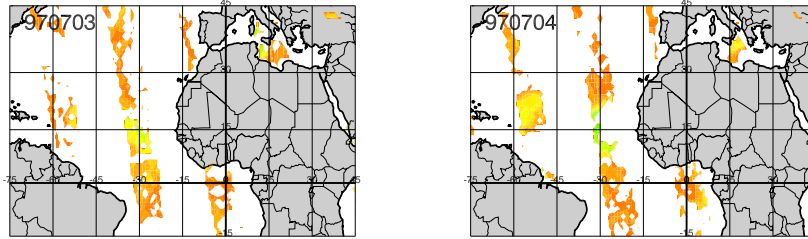AVHRR Retrieved AOD, July 3-10, 1997
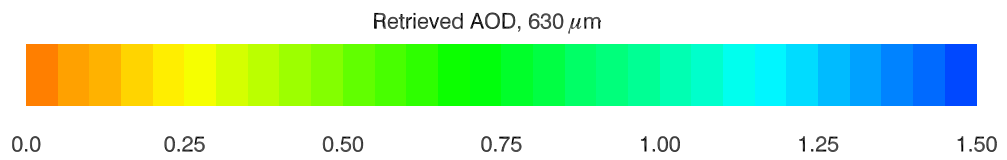
Figure 23b.

Retrieved AOD, 630 μm
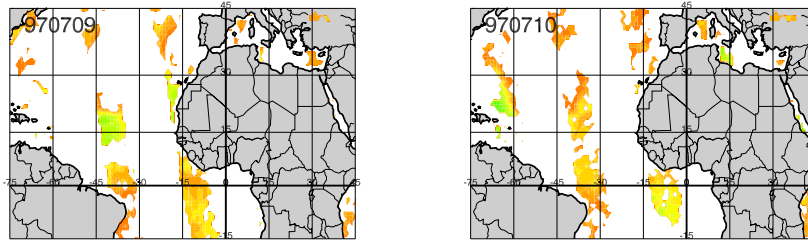
Figure 23b. AVHRR retrieved 630 nm optical depths for July 3-10.